LAWRENCE
LIVERMORE
NATIONAL
LABORATORY

LLNL-JRNL-827022

The Potential Energy Hotspot: Effects from Impact Velocity, Defect Geometry, and Crystallographic Orientation

B. W. Hamilton, M. P. Kroonblawd, A. Strachan

September 23, 2021

The Journal of Physical Chemistry C

Disclaimer

The Potential Energy Hotspot: Effects from Impact Velocity, Defect Geometry, and Crystallographic Orientation

Brenden W. Hamilton[1], Matthew P. Kroonblawd[2], Alejandro Strachan[1]*

[1]School of Materials Engineering and Birck Nanotechnology Center, Purdue University, West Lafayette, Indiana, 47907 USA
[2]Physical and Life Sciences Directorate, Lawrence Livermore National Laboratory, Livermore, California 94550, United States
*strachan@purdue.edu

Abstract

In energetic materials, the localization of energy into "hotspots" is known to dictate the initiation of chemical reactions and detonation. Recent all-atom simulations have shown that more energy is localized as internal potential energy (PE) than can be inferred from the kinetic energy (KE) alone. The mechanisms associated with pore collapse and hotspot formation are known to depend on pore geometry and dynamic material response such as plasticity. Therefore, we use molecular dynamics (MD) simulations to characterize shock-induced pore collapse and the subsequent formation of hotspots in TATB, a highly anisotropic molecular crystal, for various defect shapes, shock strengths and crystallographic orientations. We find that the localization of energy as PE is consistently larger than the KE in cases with significant plastic deformation. An analysis of MD trajectories reveals the underlying molecular- and crystal-level process that govern the effect of orientation and pore shape on PE localization. We find that the regions of highest PE relate to the areas of maximum plastic deformation, while KE is maximized at the point of impact. Comparisons against HMX reveal less energy localization in TATB, which could be a contributing factor to the latter's insensitivity.

1. Introduction

Shockwave-induced chemistry can result in a myriad of processes such as detonation[1–3], the formation of pre-biotic compounds that may have contributed to the formation of life on Earth,[4–8] and the synthesis of new materials and phases[9–11]. Often, shock-induced chemistry is triggered or enhanced by energy localization into hotspots that form as the shockwave interacts with the material's microstructure[12]. In the case of energetic materials, hotspots of sufficient size and temperature can become critical and transition into deflagration waves and eventually lead to detonation. Several mechanisms can result in the formation of hotspots, but the collapse of porosity is known to dominate the initiation of energetic materials. This was first shown through shock desensitization experiments where high explosives (HEs) were rendered insensitive after an initial weak shock caused the collapse of porosity without igniting significant amounts of material.[13] The inclusion of inhomogeneities via silica micro-beads and cavities via micro-balloons in gelled nitromethane also demonstrated the superiority of the latter in triggering detonations, decreasing the run to detonation.[14]

Significant efforts have been devoted to understanding the formation, nature, and criticality of hotspots. Physics-based scaling laws for planar void collapse supported by atomistic simulations predicted a theoretical maximum temperature achieved during pore collapse and highlighted the importance of material expansion into the void, maximizing pressure-volume work during recompression.[15] Recent molecular dynamics (MD) simulations have shown that diamond shaped voids, elongated along the shock direction, result in larger and hotter hotspots than equiaxed pores.[16] This is due to focusing of shockwave energy at the tip of the diamond, leading to molecular jetting and the formation of a low density expanding plume. Volumetric work done to recompress the plume achieves temperature values close to the maximum predicted in Ref. 15. Three-dimensional calculations of the collapse of spherical and octahedron-shaped pores in HMX (octahydro-1,3,5,7-tetranitro-1,3,5,7-tetrazocine) showed only a nominal difference in temperature[17], however pores were limited to 8nm in the shock direction which would limit molecular jetting[16]. Continuum modeling techniques have been used to explore pore aspect ratio[18] and the resultant shear banding[19] in HMX pore collapse simulations, and compared HMX and TATB[20] (1,3,5-triamino-2,4,6-trinitrobenzene). In recent years, the computational efficiency of all-atom simulations has enabled direct scale bridging with grain-scale models, opening new routes to parameterize and validate the accuracy of those models for predicting shock induced pore collapse.[21–23]

Atomic-level understanding of shock induced chemistry was greatly increased by the development of reactive force fields, such as ReaxFF, which allowed for explicit simulation of shock ignition and thermal decomposition in solid HEs such as RDX.[24,25] ReaxFF simulations using a compressive shear protocol have been utilized to explore the interplays of mechanics on chemistry.[26,27] Reactive MD techniques such as density functional tight binding have been used to explore the chemical reactivity of TATB under thermal and shock loading, as well as mechanical shear induced metallization.[28–30] The extended timescales of these techniques have allowed for the prediction of reactive properties like detonation velocity and pressure[31,32], IR spectra evolution[33–35], and detailed chemical reaction pathways[36–39]. Reactive force fields have also

enabled explicit simulation of nanoscale hotspots[40] and the upscaling of chemical reaction models for mesoscale and coarse grained simulations.[41]

Quite surprisingly, reactive MD simulations have shown that nanoscale hotspots formed following the dynamical collapse of porosity are markedly more reactive than otherwise identical hotspots at the same temperature and pressure in compressed perfect crystal.[42,43] A possible explanation for this observation is that disorder and amorphization in molecular crystals can lead to accelerated reaction compared to bulk crystalline materials[44,40] and recent advances in continuum hotspot modeling have begun to include 'shear band activation' terms to address this[45]. Recent MD simulations of shock-induced pore collapse in TATB showed that significantly more energy is localized as intra-molecular potential energy (PE) than into internal temperature or kinetic energy (KE).[46] This excess PE is the result of large intra-molecular deformations that do not significantly relax on timescales comparable to the onset of exothermic chemistry. Nonreactive, hotspot thermal conduction simulations in TATB showed that hotspots formed from the collapse of 40nm pores take nearly a full nanosecond to equilibrate with the surrounding material[47]. Assessments on the decay of the PE hotspot show almost no relaxation of intra-molecular deformations within ~200ps of collapse[46], well within the typical timescale of exothermic relaxation in similar reactive pore collapse simulations[42,43].

Molecular deformations such as these can lead to mechanochemical acceleration of reactions and alter reaction pathways.[48] Recent work in RDX combining planar pore collapse with an additional shear component directly linked hotspot criticality to the level of shear loading.[49] Excess localized PE provides a plausible explanation to the puzzling difference in reactivity between dynamically and thermally generated hotspots[42] and for chemical activation through forming nanoscale shear bands.[44] For numerous other covalent molecules, intra-molecular deformation is known the accelerate reactions[50,51], delocalize electrons[1,30], and open forbidden reaction pathways[52]. The intra-molecular PE is a quantitative measure of these deformations that may enable modeling their effect on chemical kinetics[46,53]. For this study we use non-reactive simulations, where covalent bonds cannot break; this allows us to isolate the initial intra-molecular deformations leading to chemical acceleration and characterize their persistence under mechanical relaxation processes. These simulations are designed to assess how generally applicable the prior observations on the PE hotspot are. In particular, we seek to understand whether localization of energy in intra-molecular deformations arises and persists for a range of shock strengths, for porosity of different shapes, and whether the shock direction influences this behavior in materials with considerable anisotropy in their mechanical and thermal properties [21,47,53].

To address this gap in knowledge, we characterize how different pore collapse mechanisms operating at various shock strengths (e.g., viscoplastic, hydrodynamic, molecular jetting) impacts the relative intensity and shape of the hotspot as well as the partitioning of the localized energy into kinetic (temperature) and potential (molecular strain) terms. We focus here on hot spots in the insensitive HE TATB, as its layered structure[54] leads to what is perhaps the greatest mechanical and thermal anisotropy for any explosive. This enables us to explore bounding cases for the role of shock orientation on the formation of hotspots. Recent work from Lafourcade et al. showed a strong orientation dependence for deformation mechanisms in TATB under controlled strain conditions[55] that leads to analogous deformations under shock conditions[56]. For instance, compressive stresses along [100] result in an inelastic chevron-like buckling of the basal

planes, whereas resolved shear stresses along (011)-type planes results in a non-basal gliding of the planes. Under weak stresses, the TATB crystal layers will glide in-plane[55,57,58] while detonation-level shocks lead to the formation of nanoscale shear bands[44]. Analysis of dynamical axial compression simulations of TATB crystal showed that the intra-molecular strain energy (PE) was a reliable metric to distinguish between various mechanisms for plastic flow and significant anisotropy on the mechanisms of deformation localization[53]. These observations indicate that pore collapse could exhibit a high degree of effects from anisotropy as well as shock strength.

The role of TATB anisotropy in shock loading response of the perfect single crystal has been well characterized for a shock strength near 10 GPa. All-atom simulations were used to study the perfect crystal shock response in a variety of crystallographic orientations.[56] This showed significant effects on the wave structure (single vs 2-wave response), elastic wave speeds, and deformation mechanisms, which ranged from a variety of crystal level defect formations to plasticity and intense shear localization. Coupled MD and continuum simulations explored the mechanics of pore collapse for various orientations and shock speeds for cylindrical pores.[21] Strong disparity between the all-atom and the isotropic, elastic-plastic continuum models at low shock speeds highlighted the significance of anisotropic strength effects on the formation of hotspots.

Our previous work characterized the role of pore shape, size, and shock strength in hotspot formation in HMX.[16] We use identical geometries here to enable a direct comparison between TATB (considered an insensitive explosive) and HMX (a high performance material). The extreme temperatures (>7000 K) found in HMX following the collapse of diamond shaped pores elongated along the shock propagation direction corresponds well to the theoretical maximum temperature[15] and recent experimental reactive hotspot measurements from Bassett et. al.[59–61] These high temperatures are possibly related to the jetting and gasification of material into the void, which is later recompressed by the shockwave. Holian et al. showed for simple 1D shocks in a model system that jetting occurs when the energy embedded by the shock is greater than the crystal cohesive energy: $\frac{1}{2}mU_p^2 > E_{coh}$[15]. However, events such as plasticity (e.g., dislocation motion or shear banding) and shock focusing at curved surfaces can alter the local energy deposited during shock compression.

This paper assesses the localization of energy, both kinetic and potential, in TATB following the shock-induced collapse of porosity. The use of two void shapes allows us to evaluate the role of molecular jetting, hydrodynamic collapse, and viscoplastic collapse, whereas the two crystallographic orientations used bound the single-crystal plastic response[53] to elucidate the role of molecular/crystal-level processes involved in hotspot formation. We find that TATB follows the general trends observed in HMX[16] in terms of shock strength and pore shape, but with an important quantitative difference in which TATB hotspots do not reach the same extreme temperatures (7000+ K). Unlike in HMX, the temperatures achieved in TATB are only a fraction of the theoretical maximum. Our atomistic simulations provide insight about the underlying molecular processes that control the collapse mechanisms and the overall hotspot shape and temperature, with the PE hotspot strength generally determined by the level of plastic work present. We find that the mechanisms in play, discussed below, may also be a contributing factor to the insensitivity of TATB. Finally, we find that in all cases with significant plastic flow, more energy in hotspots is stored as PE than as KE.

2. Methods

MD simulations were conducted using the LAMMPS package[62] and a validated version of a non-reactive, non-polarizable force field for TATB.[63] The force field includes tailored harmonic bond stretch and angle bend terms for flexible molecules[64], RATTLE constraints that fix the N-H bonds to their equilibrium values,[65] and an intramolecular O-H repulsion term that was implemented as a bonded interaction.[66] The covalent bond vibrations, angle bends, and improper dihedrals were modeled using harmonic functions. Proper dihedrals were modeled using a cosine series. Van der Waals interactions were modeled using the Buckingham potential (exponential repulsion and a r^{-6} attractive term) combined with short-ranged r^{-12} potentials that compensate for the divergence in the Buckingham potential at small separation. The non-bonded terms were evaluated in real space within an 11 Å cutoff. Electrostatic interactions were calculated between constant partial charges located on the nuclei and were evaluated using the short-ranged Wolf potential with a damping parameter of 0.2 $Å^{-1}$ and an 11 Å cutoff.[67] All intra-molecular non-bonded interactions are excluded by design, which allows for rigorous separation of inter- and intra-molecular potential energy terms.

Nearly orthorhombic simulation cells were prepared using the generalized crystal-cutting method[68] starting from the triclinic $P\bar{1}$ TATB crystal structure[54] with lattice parameters determined with the TATB FF at 300 K and 1 atm. For orientations denoted as (001), the crystal was oriented such that [100] was aligned with x, [120] was nearly parallel to y, and the normal to the basal planes $\mathbf{N}_{(001)} = \mathbf{a} \times \mathbf{b}$ was aligned with z, the shock direction. For the (100) orientation, $\mathbf{N}_{(100)} = \mathbf{b} \times \mathbf{c}$ was aligned with z, and the x axis was aligned with [001] (lattice vector c). For cylindrical pores with circular cross-sections, a diameter of 40 nm was used with a the axis of symmetry along x, centering the void in the geometric center of a cell. For diamond shaped pores (also cylindrical with axis along x), the diamond was cut with the long axis aligned with the shock direction (z) and the short axis aligned with the y direction (the simulation is thin in the x direction). The length was 40 nm, and its maximum width was 8 nm. Renderings of both defect shapes and the utilized crystallographic orientations are displayed in Figure 1.

Free surfaces were generated normal to the shock direction (z) by adding a 5 nm region of vacuum that removes the periodicity in that direction to prevent self-interactions. Periodic boundaries were utilized in both non-shock directions. The thermalized systems were equilibrated at 300 K using a 25 ps isothermal-isochoric (NVT ensemble) simulation with a Nose-Hoover-style thermostat and a 0.5 fs timestep.[69] To accelerate the equilibration of the system after the free surfaces were created, during the first 2.5 ps, atomic velocities were re-initialized stochastically from the Maxwell-Boltzmann distribution every 0.5 ps and were rescaled to the target temperature every 0.05 ps to attenuate breathing modes incurred by the surface tension. These configurations were used as the starting point for reverse ballistic shock simulations using adiabatic MD (NVE ensemble) with a 0.2 fs timestep. In the reverse ballistic setup,[70] the piston velocity, U_p, was added to the thermal velocities of the atoms leading to impact on the rigid piston that generates a shock front traveling through the sample in the opposite direction at the shock speed, U_s. Molecules with center of mass positions with $z \leq 1.5$ nm were held fixed throughout

the shock simulation to simulate the rigid and infinitely massive piston. We ran shock simulations at U_p = 0.5, 1.0, 1.5, and 2.0 km/s for each pore shape and crystal orientation case yielding a total of 16 simulations.

Simulation trajectories were analyzed on a molecule-by-molecule basis. The molecular center of mass (CM) positions and velocities were computed as weighted sums over all 24 atoms in each molecule. The total molecular kinetic energy KE_{tot}, and the separate contributions from the molecular translational KE_{trans}, and roto-librational and vibrational $KE_{ro\text{-}vib}$ degrees of freedom were computed as

$$K_{tot} = \sum \frac{1}{2} m_i \mathbf{v}_i \cdot \mathbf{v}_i$$

and

$$K_{trans} = \frac{1}{2} M \mathbf{V} \cdot \mathbf{V}$$

and

$$K_{ro-vib} = K_{tot} - K_{trans}$$

where lowercase variables represent mass and velocity of individual atoms and capital letter represent CM (molecular) values. The ro-vib kinetic energies $KE_{ro\text{-}vib}$ were interpreted as the molecular temperature T and were scaled to Kelvin units through

$$K_{ro-vib} = \frac{63}{2} k_B T$$

where k_B is the Boltzmann constant and the factor of 63 arises from the 3 roto-librational and 60 unconstrained vibrational degrees of freedom in the TATB molecule. The intra molecular PE is defined as

$$PE_{intra} = \sum PE_{bond} + \sum PE_{ang} + \sum PE_{dih} + \sum PE_{imp}$$

where each of the PE terms is summed over the total number of bonds/angles/dihedrals in the molecule and are described by the harmonic, cosine series, and tabulated terms of the forcefield[63] described at the beginning of Section 2. All molecular properties were locally averaged within a sphere 1.5 nm in radius about each molecule CM to smooth fluctuations.

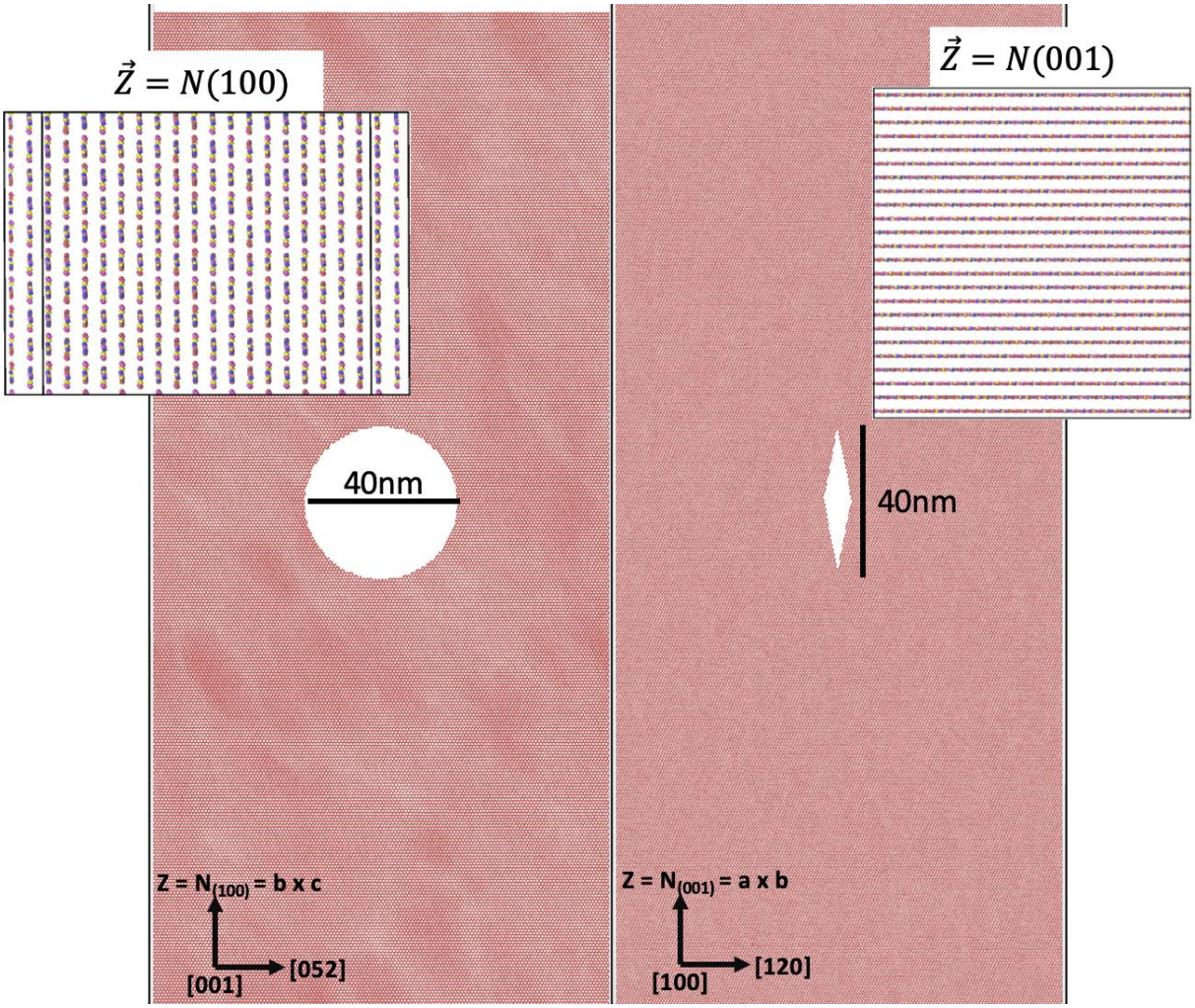

Figure 1: Simulation set up for shock interaction with a cylindrical pore (left) and a diamond (right) pore elongated along the shock direction, inset figures display the two crystallographic orientations studied for both pores. Shocks propagate from bottom to top, with periodic boundary conditions in the other two directions.

3. Crystal Level Processes of Pore Collapse

3.1 Cylindrical Pores with Circular Cross-sections

We begin by assessing the collapse of porosity at molecular and crystal-level scales, looking specifically at the structure of the collapsing material, as this can heavily influence the shape, size, and strength of the hotspot[16,23]. Assessing just the cylindrical pores first, see Figure 2, the general shape of the collapsing material only shows minor dependence on the crystal orientation (row 1 vs row 2 in Figure 2), but as expected, strong dependence on shock strength (various columns of Figure 2). For U_p=0.5 km/s, cylindrical pores collapse laterally via a viscoplastic process driven by the compressive stresses following the passage of the shock. With increasing shock strength, the collapse transitions to a hydrodynamic regime where the upstream surface expands

into the void on a time scale similar to the passage of the shock. In this regime, the stresses involved are significantly higher than the material strength[53,55,71] and the deforming material behaves approximately like a fluid (hence the name hydrodynamic).

In the case of a hydrodynamic collapse, the material is often assumed to have little to no strength. From this, as could be expected, the collapsing material under (100) shocks appears to be amorphized by the fast plastic deformation, with no noticeable structure seen in Figure 2. Quite surprisingly, for (001) shocks, the collapsing material appears to retain a significant degree of crystalline order. In this case, this orientation of the crystal is significantly more compressible in the shock direction[63], and the TATB basal planes become highly deformed via intra layer sliding and non-basal gliding, as well as plane buckling, but remain locally structured. This retained structure in the basal planes is likely related to the small number of slip systems available for plastic deformation[55] in conjunction with dislocation motion instability under shock-like pressures[72] that leads to nanoscale shear banding[44,56] as a primary plastic response for this orientation.

To further characterize the structure of the collapsing material, Figure 3 displays the radial distribution functions obtained from the molecular centers of mass for both orientation's collapsing regions for the cylindrical pore and the shocked crystal for $U_p = 2.0\ km/s$, which includes some layer sliding and non-basal glide defects, which broadens peaks on top of thermal fluctuation. This clearly confirms the structural difference in the collapsing material for the two orientations. While both orientations result in mostly amorphous material in the hotspot after the collapse and recompression (Fig. 3(b)), the collapsing material is structured for the (001) and amorphous for the (100), Fig. 3(a). Differences with respect to the perfect crystal arise due to both plastic deformations and a complicated pressure gradient in the collapsing material. The different deformation paths and localization of plastic flow in these two different collapses for the 'hydrodynamic' regime at U_p = 2.0 km/s is expected to influence the characteristics of the resulting hotspot.

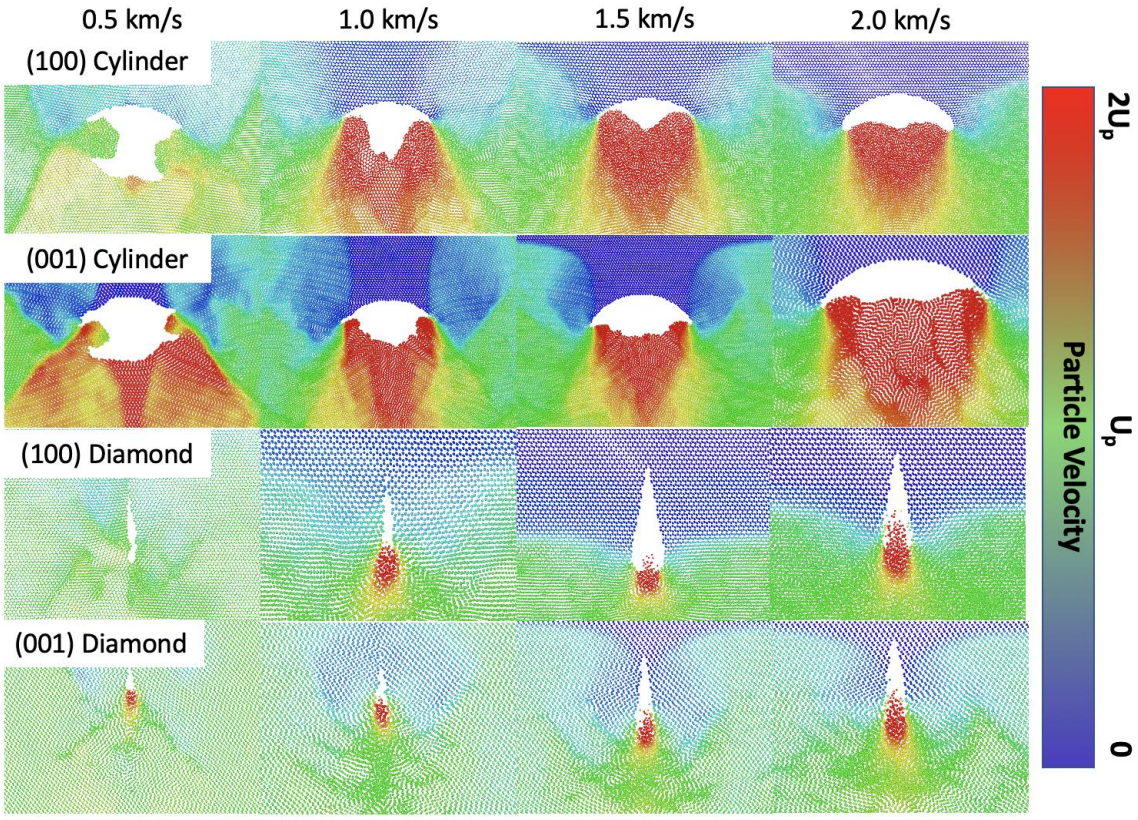

Figure 2: Molecular COM velocities in the shock direction during pore collapse. Color bar relative to initial impact velocity.

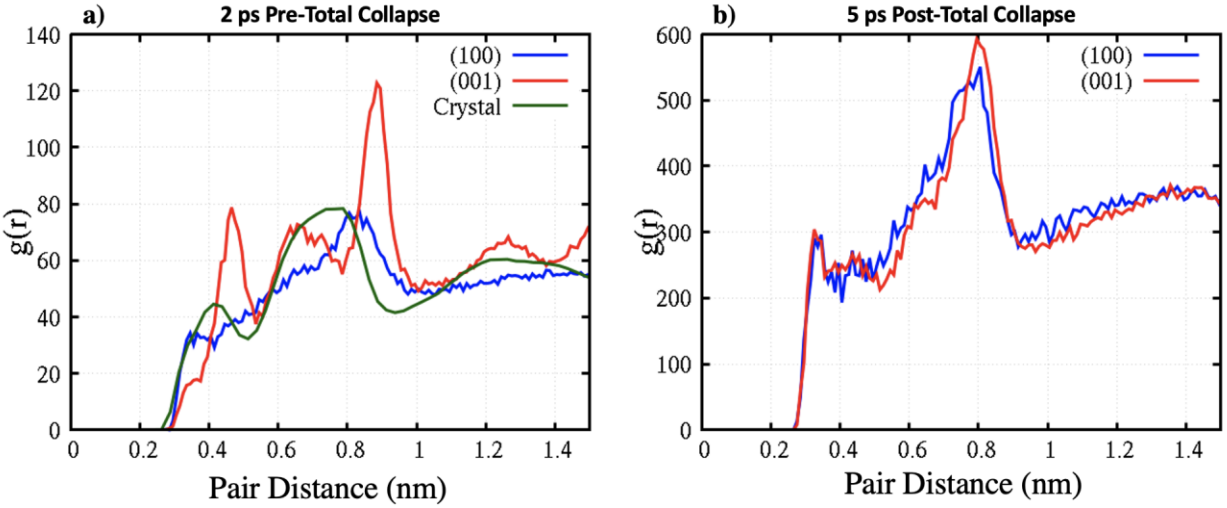

Figure 3: Radial distribution functions for the pore collapse (mid-collapse) and the hotspot, for both orientations, cylindrical void, at 2.0 km/s. Crystal g(r) represents the perfect crystal at the shock pressure for (001) with U_p = 2.0 km/s.

3.2 Cylindrical Pores with Diamond Cross-sections

In the case of the diamond shaped pores, weak shock collapses are dominated by lateral collapse, analogous to the lateral, viscoplastic collapse in circular cylinders. However, while the viscoplastic mechanism in the cylinder is dominated by plastic flow and material deformation, the high aspect ratio diamonds simply close without much plastic work being done on the surrounding material. This results in almost no discernable hotspot.

For strong shocks, the collapse process is dominated by molecular ejecta. When a shockwave reaches a flat free surface, the material expanding into vacuum travels at $2U_p$.[73] In the case of nonplanar defects, shock focusing can lead to much higher ejecta velocities[74,75]. From the anisotropic elasticity and plasticity in TATB[55] it is reasonable to anticipate that the two orientations may result in different amounts of ejecta. However, the two diamond pores exhibit similar amounts of ejecta at early times, which agrees well with the relationship from Holian et al., stating that jetting occurs when the shock energy is greater than the crystal's cohesive energy, $\frac{1}{2}mU_p^2 > E_{coh}$[15], setting the assumption that the onset of jetting should be mostly orientation independent.

The main difference between the two orientations is the location of the shock front relative to the ejecta. In the (100) case, the ejecta expands out in front of the shockwave (blue to green colored transition in Figure 2). For the (001) case, the reverse occurs, with the shock wave ahead of the ejecta. This occurs despite the shock speed of the (001) case being higher than in the (100) case, U_s of 7.02 km/s vs. 6.23 km/s[21], respectively. For the (001) shock, the ejected molecules have velocities between 4 and 6 km/s, and between 5 and 7 km/s for (100), allowing the ejecta to expand quicker. See Figure S1 in the SI for full velocity distributions.

As shown in Figure 4, both orientations have a two-wave feature. In the (100) case shown in dashed curves, the leading wave particle velocity is $U_p \cong 0.2\ km/s$ and causes almost no pressure increase. In the (001) case shown in solid curves, the leading wave is $U_p \cong 1.4\ km/s$. For (100), the trailing wave, $U_p = 2.0\ km/s$ initiates jetting, allowing the ejecta to accelerate past this wave. For the (001) case, the leading wave of $U_p \cong 1.4\ km/s$ does not promptly initiate ejecta but does significantly increase the pressure in the bulk. Ejecta do not form until the $U_p \cong 2.0\ km/s$ wave reaches the pore. Thus, the first wave initiates lateral collapse of the pore prior to ejecta formation, with the lateral collapse choking off the ejecta before it can recompress on the downstream face of the pore. For (100), the ejecta can fully expand and be fully recompressed. Renderings of the time history of both diamond collapse processes are shown in Figure S2 in the SI. These differences in material expansion history will result in different structural characteristics upon recompression that may have bearing on kinetic and potential energy localization.

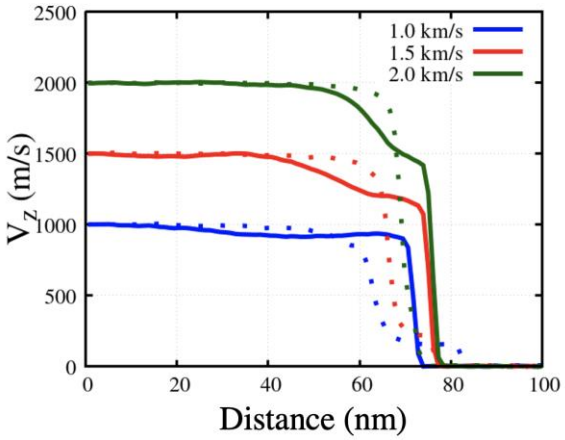

Figure 4: Wave profiles in the bulk system for each impact velocity measured with respect to unshocked material. Dashed curves represent the (100) orientation and solid curves the (001) orientation. Both systems have a 'two-wave' feature, with the (100) leading wave causing particle velocities on the order of 200 m/s, whereas the (001) leading wave leads to significant velocity (and therefore pressure) increase.

4. Temperature and Potential Energy Fields of Hotspots

Figure 5 shows molecular renderings for the various hotspots generated after pore collapse colored by both KE (left) and PE (right) in a given column, for U_p = 1.0 to 2.0 km/s. The 0.5 km/s results are omitted from this post-collapse analysis as the relative energy difference in the KE and PE hotspots formed from cylindrical pores was smaller than thermal fluctuations and the diamond pore cases produced almost no hotspot at all. Note that the color bar upper bound depends on U_p and is 100, 75, and 50 kcal/mol for the 2.0, 1.5, and 1.0 km/s cases, respectively. Each pair of columns collects a shock speed, with the left panels of each group showing temperature (in units of KE) and the right half showing intra-molecular PE. Each row corresponds to an orientation and defect pair.

We note that the significant anisotropy of TATB is manifested in the markedly different shock-induced plasticity and the associated dissipation away from the hotspot areas. This, together with the anisotropic elasticity, results in significantly higher bulk temperatures for (001) shocks as compared to (100). For example, a (001) shock with U_p = 2.0 km/s has a shock velocity of 7.0 km/s and results in a temperature increase of ~770 K, whereas a (100) shock with the same particle velocity has a U_s of 6.2 km/s and an average temperature of ~650 K, which is consistent with those found in Ref 21. In addition, (100) shocks lead to relatively homogeneous temperature fields in the bulk, whereas the (001) orientation localizes energy in shear bands, which can account for the excess temperature. Characteristic hot spot energy magnitudes and structural sizes and shapes are discussed in detail below.

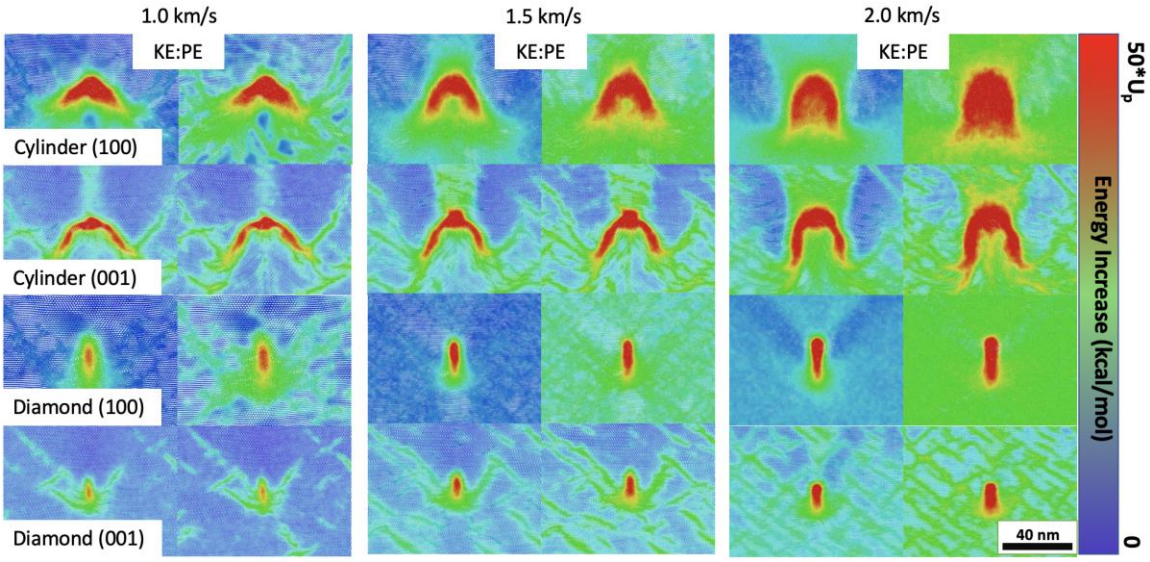

Figure 5: Molecular renderings of all hotspots at 5ps after total collapse of porosity, colored as both kinetic energy (which is proportional to temperature) and intra-molecular potential energy. Color bar relative to impact velocity (max value 50, 75, and 100 kcal/mol, for 1, 1.5, and 2 km/s respectively).

4.1 Role of pore shape and shock speed.

The potency of a hotspot is related to both its size and temperature, since the critical temperature for ignition decreases with increasing size[76]. Thus, to quantify the thermal fields of hotspots we compute the area (A) of the hotspot with temperature exceeding a value temperature (T) and plot this relationship in the T-A space. Figure 6 shows the T-A plots for cylindrical pores (6a) and diamond pores (6b) for various U_p and shock orientations; solid curves indicate (001) shocks while dotted curves denote (100) shocks. To single out the rise in temperature from the collapse of porosity, we reference the temperature field to the value corresponding bulk shock temperature, which may include heating from shear band formation in strong shock cases.

Inspection of Figure 6 shows that the collapse of diamond pores results in smaller and colder hotspots than that of cylindrical pores, except for the strongest (100) shocks where the maximum temperature resulting from the collapse of diamond pores is over 500 K higher than in the case of cylindrical pores. In our previous work comparing pore shape for HMX, Ref 16, the diamond pores showed temperatures 2-3 times larger than cylindrical pores from the rapid recompression of ejecta. In TATB, the same ejecta forms in diamond pores, however the resulting peak temperatures are much lower.

Hotspots from cylindrical pores are much larger than that of diamond pores. This is due to the significant difference in initial area, allowing for more mechanical work to occur in cylindrical collapses. Figure 7 shows the T-A plots for the $U_p = 2.0\,km/s$ cases in which the area is normalized by the original area of the pore. This normalization shows that the diamond and cylindrical pores in TATB result in roughly the same relative hotspot temperature distributions, which is in marked contrast with HMX in which diamonds were much more efficient in localizing KE[16].

Looking at peak temperatures, for weaker shocks, the cylindrical pores are much hotter than the diamonds. As can be seen from the collapse mechanisms in Figure 2, the viscoplastic collapse of cylinders undergoes much more plastic deformation than for diamond pores, resulting in hotter hotspots. As shock speed increases, the trend begins to reverse due to the presence of molecular ejecta in the diamond pores and only a hydrodynamic collapse in the cylinders. There is some disparity in these results for the different orientations that will be discussed in Section 4.2. Overall, for both shapes, hotspot size and temperature increase with increasing shock speed, as expected.

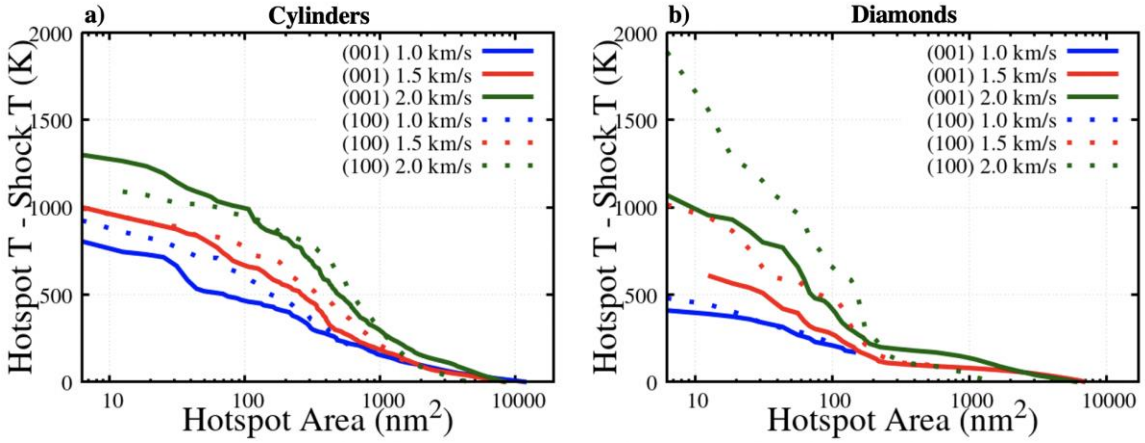

Figure 6: Temperature- Area cumulative plots for a) cylinder voids and b) diamond voids. Impact speed shown by color, orientation shown by point shape.

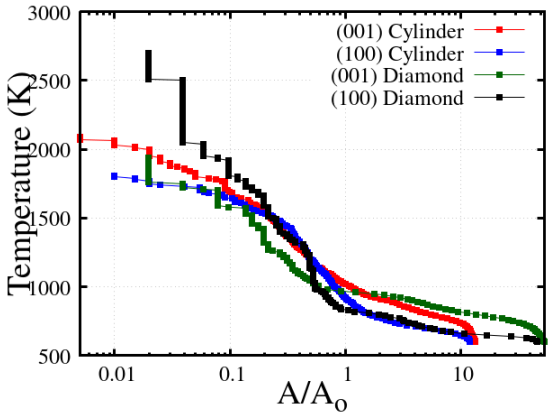

Figure 7: T-A plot (absolute temperature) for both void shapes and crystal orientations, at 2.0 km/s impact speed.

4.2 Role of shock orientation

Due to their significant disparity in initial shape, we assess the role of crystallographic orientation on hotspot formation for the cylindrical and diamond pores separately. Starting with the two cylindrical pore crystal orientation cases, it is evident that, despite their similar temperature-area plots (Figure 6a), the temperature fields command highly dissimilar shapes

(see Figure 2). The (100) shock direction cylindrical pore collapse results in a rather equiaxed hotspot, indicative of the initial void shape. However, the (001) shocks result in a crescent-shaped hotspot, with a discernable 'core' (top center) and 'legs' (lower flanks). While the maximum temperatures and extent of the energy localization are similar for the two shock directions (see Figure 3a), differences in the initial temperature fields and post-shock densities can result in different thermal dissipation rates[47] and may exhibit different thresholds for reaction/deflagration. Thus, the criticality of the hotspots following the collapse of such pores can be expected to depend on shock direction. These observations also apply for lower shock speeds, but the difference is most evident in the hydrodynamic cases.

The crystal scale processes (e.g., intense shearing and plasticity) that create these differing shapes stems from the fully hydrodynamic collapse of the (100) case and the retained crystal structure in the (001), as shown in Figures 2 and 3. As is seen in a majority of high explosives, the hydrodynamic collapse leads to a unform, circular hotspot[18,23,42,43,56]. The (001) collapse features the ordered material impacting on the downstream face of the pore and highly sheared material which flank the collapsing material. These sheared regions result in the long 'legs' of the crescent shape as shown in Figure 6. As shown in Figure 2, the (100) cases begin to act more hydrodynamic at lower U_p, leading to the slightly higher temperatures seen in Figure 6a, whereas the shear localization along of the (001) case at higher Up leads to a higher peak temperature, with very similar respective areas for all speeds.

For weak shocks, little discernable difference exists in the hotspots formed from diamond pores. At higher speeds, the (100) direction diamond pore hotspots reach significantly higher temperatures and areas. As discussed in Section 3.2 and shown in SM-2, the two-wave feature of the (001) direction leads to lateral collapse of the pore prior to ejecta being able to fully expand and recompress. The choked off ejecta of the (001) case cannot generate as much mechanical work as the (100) case, leading to lower temperatures. Additionally, since the ejecta cannot extend across the longitudinal length of the pore, the (001) hotspot itself covers less total area.

4.3 Localization of potential energy

We now focus on the localization of energy in PE following the collapse of porosity, assessing any differences in trends from that of the temperature description of the hotspot. Figure 8 shows PE vs cumulative Area (PE-A) plots for intra-molecular potential energy that are analogous to the T-A plots in Figure 6. We find that the trends described above for the temperature fields (in terms of role of shock strength, orientation, and pore shape) mostly apply to the localization of PE but some important differences should be highlighted.

While the maximum temperature of the (001) cylindrical pore was greater than that of the (100) case, the difference in PE is significantly larger. The difference is so substantial that the peak PE values for the 1.5 km/s (001) shock surpass the 2 km/s (100) shock at very small areas (Figure 8a). This is most likely a result of the significant shear localization at the sides of the pore collapse in the (001) cylinder leading to highly deformed molecules, similar to the formation of shear bands[44].

The T-A curve shown in Figure 6(a) for the (100) cylindrical pore with $U_p = 1.5\ km/s$ is slightly higher than that for the (001) shock at small areas, and considerably higher at larger areas. However, this trend reverses in terms of PE in Figure 8(a), with the (001) shock cylindrical pore collapse leading to a slightly "hotter" hotspot in PE terms for all areas. This is indicative of a

loading path dependence in how hotspot energy partitions between KE and PE. In Section 5, we will more closely inspect the PE-T distributions for all cases at early times for which disparity in KE and PE is largest.

The T-A and PE-A trends are relatively closer in the case of diamonds in which significantly less plastic flow occurs. This may be attributable to the difference in initial area or the dissimilar collapse mechanisms.

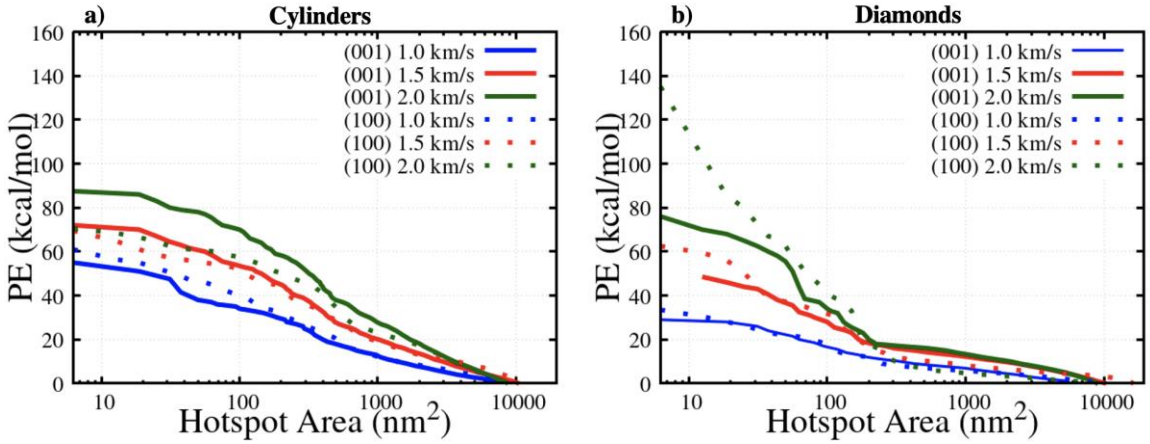

Figure 8: PE-A plot for cylinder and diamond pores. Organized the same as Figure 6, with the y axis correspond 0-2200 in temperature units.

5. PE-T Distributions

Reference 46 established that hotspots are not fully described by their KE fields; the energy localized as PE cannot be inferred from the KE and the mapping is not one-to-one. The hotspots analyzed in Section 4 show a wide range of PE and temperature states for various pore shapes and shock strengths. In this section, we quantify the relationship between PE and temperature for all the cases studied to assess the role of shock strength, orientation, and defect shape on the disparity between the two energies.

Figure 9 displays scatter plots of local PE vs. temperature for the various hotspots right after total collapse of the void (t_o + 1 ps). These plots are broken into four subsets based on shock orientation and defect shape. The data represents the entire system at a single snapshot in time, and thus shows the unshocked state (low PE and temperature), the shocked states at a range of times behind the leading wave, and the hotspot. Dashed lines represent classical equipartition of energy.

As expected, the total PE and temperature are lower for weaker shocks, as is the spread of PE states for a given temperature. For weaker shocks, the system closely follows equipartition in which energy is equally shared between degrees of freedom that appear as quadratic terms in the Hamiltonian, which leads to approximately equal KE and thermal PE. We find a strikingly broad distribution of PE states in the case of cylindrical pores, while collapsed diamonds show a simpler relationship between PE and T, in which they mostly follow equipartition of energy. In the case of the cylindrical pores, the spread of PE states for a given temperature is most

noticeable at mid temperatures (>800 K for U_p = 2.0 km/s). Quite interestingly, (001) shocks result in two distinct PE branches while the (100) shocks exhibit a high PE hump at intermediate hotspot temperatures, with almost all points existing in excess PE as compared to classical equipartition of energy (dashed black lines in Figure 9). The lack of excess in PE for the diamond pores is most likely related to the lack of plastic flow, which larger diamonds could plausibly still induce.

In order to understand the processes that result in the high-PE states, corresponding to highly deformed molecules, we map the molecules corresponding to the high-PE branch in the 2 km/s (001) and the hump in the 2 km/s (100) into real space, see Figure 10. This shows that, in both cases, the high-PE states do not correspond spatially to the impact plane where the expanding material collides with the downstream face of the pore. Rather, they correspond to the areas directly behind this, which have the highest degree of plastic deformation. This observation explains why the diamond pores do not show high PE states for a given KE, as little plastic flow is needed to fill the void space. The initial location plots of the various colored atoms from Figure 10 are available in Figure S3 in the SI. In which most of the black areas are in front of the pore and the red are the rim of the pore.

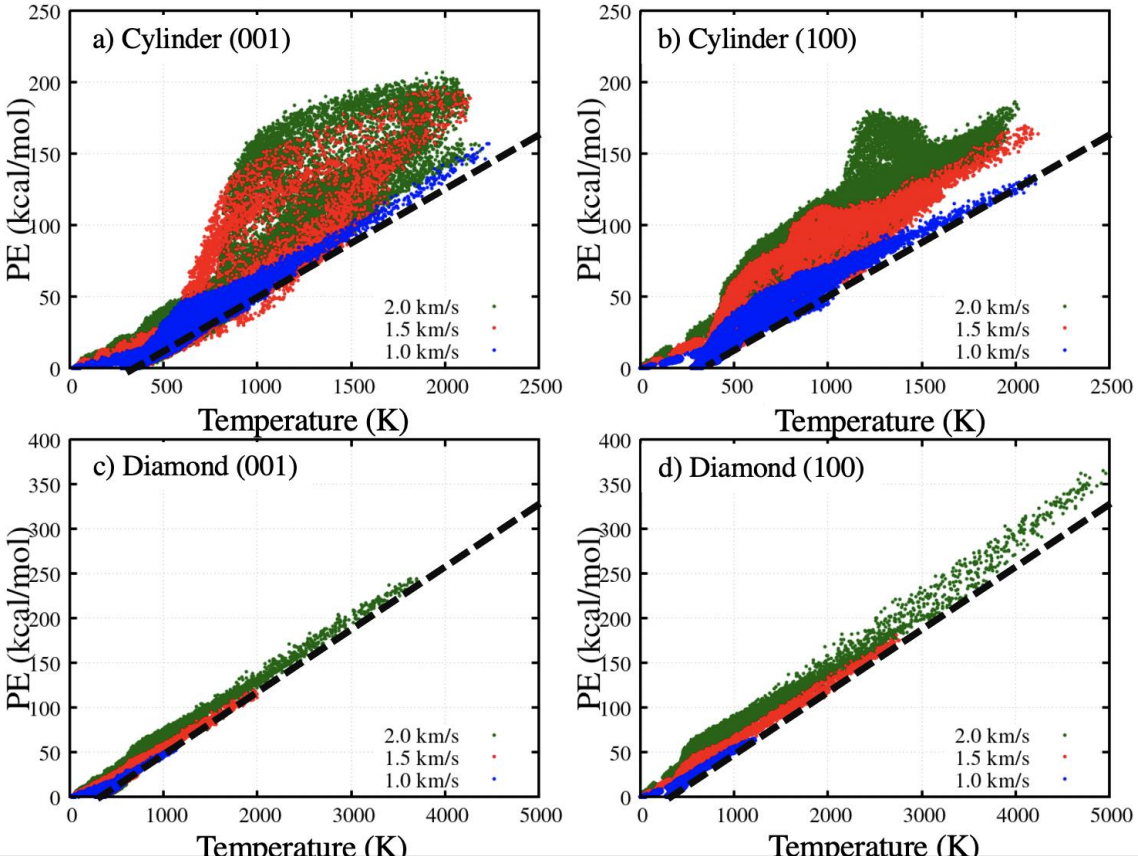

Figure 9: PE – Temperature plots for all the hotspots for all 4 orientation/shape cases where PE is the rise in intramolecular PE from the unshocked 300 K state. The labels on each plot designate the defect shape, shock direction. Color designates shock strength. Distributions taken at t_o + 1.0 ps. Dashed lines represent classical equipartition of energy.

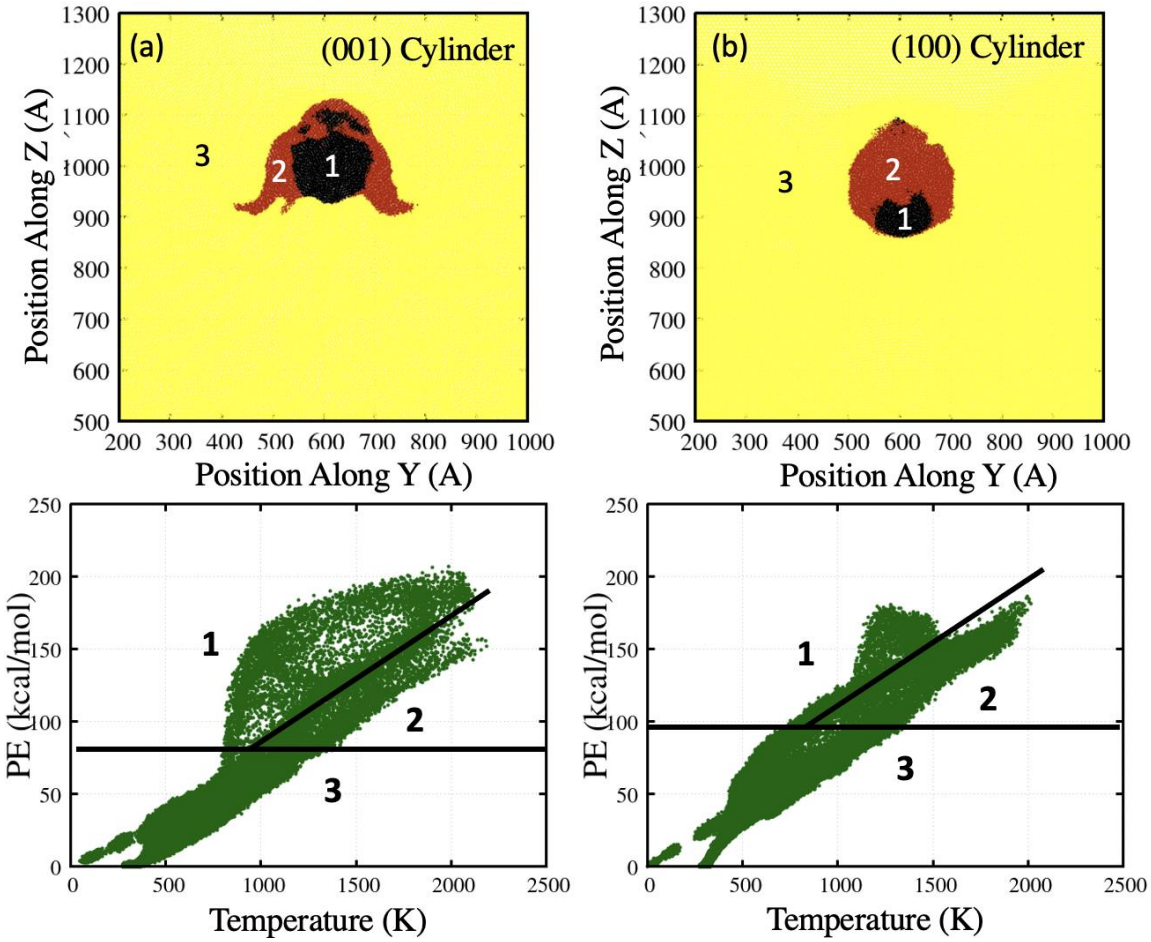

Figure 10: Spatial location of the molecules of the 2.0 km/s cylindrical pore collapses. Bottom panels show the PE(T) distributions from Figure 9, with 3 regions depicted that are colored appropriately in the spatial plot with region 1 in the black, region 2 in red, and region 3 in yellow.

6. Energy Localization Efficiency: TATB vs HMX

Figure 11 compares the temperature fields (T vs. cumulative area plots) resulting from the collapse of pores in TATB and HMX for 2.0 km/s. Note that the HMX results are for 40nm diamond and cylindrical pores from Ref. 16. For all cases the area is scaled by the initial defect area for the pores and we scale the temperature rise ($T_{shock} - T_{bulk}$) by the theoretical maximum hotspot temperature from Ref 15: $k_B \Delta T = \frac{m}{3} U_s U_p$ where m is the mass of the molecule. As shown in Figure 7, TATB pores have similar efficiency at localizing energy, except for a (100) shock with a diamond pore, where we find higher temperatures. The collapse of cylindrical pores in HMX result in hotspots with similar temperature distributions to TATB. However, Figure 11 shows that diamond pores result in significantly higher temperatures in HMX than in TATB.

Using the cohesive energy scaling law for jetting from Holian et. al. in Ref 15, $\frac{1}{2} m U_p^2 > E_{coh}$ (see section 3.2), we can compare E_{coh} / m (where m is taken to be the molecular weight) as an assessment of each material's propensity to jet. For TATB and HMX respectively, this value is 6.7

x 10^{-3} and 6.9 x 10^{-3} (eV/molecule), or more coherently, the necessary U_p to jet is 1.14 and 1.15 km/s for TATB and HMX, respectively. However, the energy localized from diamond pores is greater for HMX than for either orientation in TATB. Another key difference is that the velocities of jetted HMX molecules are significantly higher than either of the TATB orientations. SM-1 shows the distributions of molecular center of mass velocities for jetted molecules in both 2.0 km/s diamond cases and an HMX 40nm diamond from Ref. 16. Despite similar E_{coh} / MW values, jetted HMX molecules possess much higher KE for equivalent shock and defect conditions. This indicates that jetting, which may be key to high temperature hotspots seen experimentally[59–61], is the result of not just the cohesive properties of the crystal, but complex microstructural phenomena related to crystal defects and stress relaxation mechanisms. The present results indicate that jetting by itself serves mostly to increase the KE of a hotspot and does not lead to significant differences in the localization of PE on the length scales studied here.

These results widen a few questions regarding TATB: Do TATB crystalline defects and shear bands alleviate more energy in the bulk than HMX, causing less violent pore collapse and weaker hotspots? Here we show a lower efficiency in generating hotspots in TATB relative to HMX, which may help to account for insensitivity to shock initiation that is typically rationalized by molecular and chemical traits such as covalent clustering reactions[77,78] and the crystal's strong 2D hydrogen bonding network[30,79]. The overall mechanisms behind molecular jetting and massive hotspot temperatures are still not fully understood, but obviously play a significant role in the criticality of hotspots and the overall thermo-mechanical response of a material under shock loading.

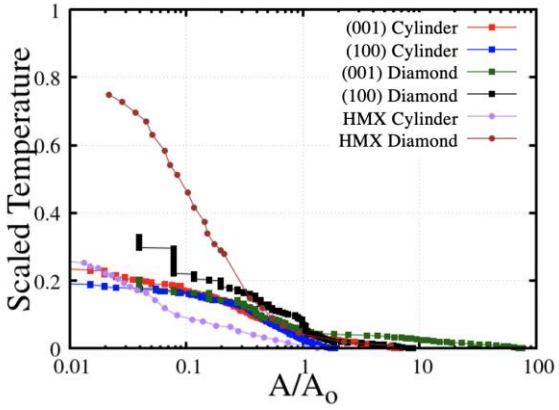

Figure 11: Scaled Temperature-Area plots for shocks, and 2 HMX shocks from Ref 16.

7. Conclusions

In summary, we have shown that the greater localization of intra-molecular potential energy (PE) than kinetic energy (KE) occurs in TATB for a variety of impact velocities, defect shapes, and crystallographic orientations. This shows that the results of Ref. 46 are a more general finding for a variety of shock states. Within each orientation, the trends seen in PE are nearly the same as those seen in temperature, with excess PE in cases with significant plastic flow. Between orientations, the difference in hotspot shape and size can be broadly explained by the molecular and crystal-level processes occurring during the collapse such as shear localization and lateral relaxations of the shocked crystal. For cylindrical pores, both hotspots reach similar temperatures

and total areas. However, for diamond pores, while both orientations lead to significant molecular spall, an orientation dependence temperature is evident. We show this results from the shockwave progressing past the far end of the diamond pore prior to spallation in some cases, which causes lateral compression of the diamond pore that chokes off the jetted material and limits the maximum hotspot temperature. For all strong shock cases in cylindrical pores ($U_p \geq 1.5$ km/s), there is no direct mapping between the KE and PE of the hotspot, implying that the thermodynamic state of the hotspot cannot be characterized by temperature alone. Lastly, we compare scaled hotspot temperatures in TATB to previous results for HMX, showing a potential inefficiency of TATB to creating high-temperature hotspots from mechanisms such as molecular ejecta. This result opens new questions about the general role of crystal-level defect formation in forming hotspots and how microstructure and crystallography affect shock focusing at defects, especially in cases of molecular ejecta.

Acknowledgements

This work was supported by the Laboratory Directed Research and Development Program at Lawrence Livermore National Laboratory, project 18-SI-004 with Lara Leininger as P.I. Partial support was received from the US Office of Naval Research, Multidisciplinary University Research Initiatives (MURI) Program, Contract: N00014-16-1-2557. Program managers: Chad Stoltz and Kenny Lipkowitz. Simulations were made possible by computing time granted to MPK through the LLNL Computing Grand Challenge, which is gratefully acknowledged. This work was performed under the auspices of the U.S. Department of Energy by Lawrence Livermore National Laboratory under Contract DE-AC52-07NA27344. It has been approved for unlimited release under document number LLNL-JRNL-827022.

References

(1) Reed, E. J.; Manaa, M. R.; Fried, L. E.; Glaesemann, K. R.; Joannopoulos, J. D. A Transient Semimetallic Layer in Detonating Nitromethane. *Nat. Phys.* **2008**, *4* (1), 72–76.

(2) Bastea, S. Nanocarbon Condensation in Detonation. *Sci. Rep.* **2017**, *7* (November 2016), 1–6.

(3) Reed, E. J.; Rodriguez, A. W.; Manaa, M. R.; Fried, L. E.; Tarver, C. M. Ultrafast Detonation of Hydrazoic Acid (HN 3). *Phys. Rev. Lett.* **2012**, *109* (3), 1–5.

(4) Goldman, N.; Tamblyn, I. Prebiotic Chemistry within a Simple Impacting Icy Mixture. *J. Phys. Chem. A* **2013**, *117* (24), 5124–5131.

(5) Goldman, N.; Reed, E. J.; Fried, L. E.; William Kuo, I. F.; Maiti, A. Synthesis of Glycine-Containing Complexes in Impacts of Comets on Early Earth. *Nat. Chem.* **2010**, *2* (11), 949–954.

(6) Martins, Z.; Price, M. C.; Goldman, N.; Sephton, M. A.; Burchell, M. J. Shock Synthesis of Amino Acids from Impacting Cometary and Icy Planet Surface Analogues. *Nat. Geosci.* **2013**, *6* (12), 1045–1049.

(7) Kroonblawd, M. P.; Lindsey, R. K.; Goldman, N. Synthesis of Functionalized Nitrogen-Containing Polycyclic Aromatic Hydrocarbons and Other Prebiotic Compounds in Impacting Glycine Solutions. *Chem. Sci.* **2019**, *10* (24), 6091–6098.

(8) Steele, B. A.; Goldman, N.; Kuo, I. F. W.; Kroonblawd, M. P. Mechanochemical Synthesis of Glycine Oligomers in a Virtual Rotational Diamond Anvil Cell. *Chem. Sci.* **2020**, *11* (30), 7760–7771.

(9) Shen, Y.; Reed, E. J. Quantum Nuclear Effects in Stishovite Crystallization in Shock-Compressed Fused Silica. *J. Phys. Chem. C* **2016**, *120* (31), 17759–17766.

(10) Shen, Y.; Jester, S. B.; Qi, T.; Reed, E. J. Nanosecond Homogeneous Nucleation and Crystal Growth in Shock-Compressed SiO2. *Nat. Mater.* **2016**, *15* (1), 60–65.

(11) Armstrong, M. R.; Lindsey, R. K.; Goldman, N.; Nielsen, M. H.; Stavrou, E.; Fried, L. E.; Zaug, J. M.; Bastea, S. Ultrafast Shock Synthesis of Nanocarbon from a Liquid Precursor. *Nat. Commun.* **2020**, *11* (1), 1–7.

(12) Hamilton, B. W.; Sakano, M. N.; Li, C.; Strachan, A. Chemistry Under Shock Conditions. *Annu. Rev. Mater. Res.* **2021**, *51* (1), 101–130.

(13) Campbell, A. W.; Travis, J. R. The Shock Desensitization of Pbx-9404 and Composition B-3. *Los Alamos Natl. Lab.* **1985**, No. LA-UR-85-114.

(14) Dattelbaum, D. M.; Sheffield, S. A.; Stahl, D. B.; Dattelbaum, A. M.; Trott, W.; Engelke, R. Influence of Hot Spot Features on the Initiation Characteristics of Heterogeneous Nitromethane. *Int. Detonation Symp.* **2010**, *LA-UR-10-0*.

(15) Holian, B. L.; Germann, T. C.; Maillet, J. B.; White, C. T. Atomistic Mechanism for Hot Spot Initiation. *Phys. Rev. Lett.* **2002**, *89* (28), 1–4.

(16) Li, C.; Hamilton, B. W.; Strachan, A. Hotspot Formation Due to Shock-Induced Pore Collapse in 1,3,5,7-Tetranitro-1,3,5,7-Tetrazoctane (HMX): Role of Pore Shape and Shock Strength in Collapse Mechanism and Temperature. *J. Appl. Phys.* **2020**, *127* (17).

(17) Long, Y.; Chen, J. Theoretical Study of the Defect Evolution for Molecular Crystal under Shock Loading. *J. Appl. Phys.* **2019**, *125* (6).

(18) Springer, H. K.; Bastea, S.; Nichols, A. L.; Tarver, C. M.; Reaugh, J. E. Modeling The Effects of Shock Pressure and Pore Morphology on Hot Spot Mechanisms in HMX. *Propellants, Explos. Pyrotech.* **2018**, *43* (8), 805–817.

(19) Austin, R. A.; Barton, N. R.; Reaugh, J. E.; Fried, L. E. Direct Numerical Simulation of Shear Localization and Decomposition Reactions in Shock-Loaded HMX Crystal. *J. Appl. Phys.* **2015**, *117* (18).

(20) Rai, N. K.; Sen, O.; Udaykumar, H. S. Macro-Scale Sensitivity through Meso-Scale Hotspot Dynamics in Porous Energetic Materials: Comparing the Shock Response of 1,3,5-Triamino-2,4,6-Trinitrobenzene (TATB) and 1,3,5,7-Tetranitro-1,3,5,7-Tetrazoctane (HMX). *J. Appl. Phys.* **2020**, *128* (8), 1–24.

(21) Zhao, P.; Lee, S.; Sewell, T.; Udaykumar, H. S. Tandem Molecular Dynamics and Continuum

Studies of Shock-Induced Pore Collapse in TATB. *Propellants, Explos. Pyrotech.* **2020**, *45* (2), 196–222.

(22) Duarte, C. A.; Li, C.; Hamilton, B. W.; Strachan, A.; Koslowski, M. Continuum and Molecular Dynamics Simulations of Pore Collapse in Shocked β -Tetramethylene Tetranitramine (β -HMX) Single Crystals . *J. Appl. Phys.* **2021**, *129* (1), 015904.

(23) Wood, M. A.; Kittell, D. E.; Yarrington, C. D.; Thompson, A. P. Multiscale Modeling of Shock Wave Localization in Porous Energetic Material. *Phys. Rev. B* **2018**, *97* (1), 1–9.

(24) Strachan, A.; van Duin, A. C. T.; Chakraborty, D.; Dasgupta, S.; Goddard, W. A. Shock Waves in High-Energy Materials: The Initial Chemical Events in Nitramine RDX. *Phys. Rev. Lett.* **2003**, *91* (9), 7–10.

(25) Strachan, A.; Kober, E. M.; Van Duin, A. C. T.; Oxgaard, J.; Goddard, W. A. Thermal Decomposition of RDX from Reactive Molecular Dynamics. *J. Chem. Phys.* **2005**, *122* (5).

(26) Zybin, S. V.; Goddard, W. A.; Xu, P.; Van Duin, A. C. T.; Thompson, A. P. Physical Mechanism of Anisotropic Sensitivity in Pentaerythritol Tetranitrate from Compressive-Shear Reaction Dynamics Simulations. *Appl. Phys. Lett.* **2010**, *96* (8), 1–4.

(27) Guo, D.; An, Q.; Goddard, W. A.; Zybin, S. V.; Huang, F. Compressive Shear Reactive Molecular Dynamics Studies Indicating That Cocrystals of TNT/CL-20 Decrease Sensitivity. *J. Phys. Chem. C* **2014**, *118* (51), 30202–30208.

(28) Riad Manaa, M.; Reed, E. J.; Fried, L. E. Atomistic Simulations of Chemical Reactivity of TATB under Thermal and Shock Conditions. *Proc. - 14th Int. Detonation Symp. IDS 2010* **2010**, 837–843.

(29) Manaa, M. R.; Goldman, N.; Fried, L. E. Simulation of Cluster Formation in Overdriven and Expanding TATB by Molecular Dynamics. *Proc. 15th Int. Detonation Symp.* **2015**, 53–59.

(30) Manaa, M. R. Shear-Induced Metallization of Triamino-Trinitrobenzene Crystals. *Appl. Phys. Lett.* **2003**, *83* (7), 1352–1354.

(31) Hamilton, B. W.; Kroonblawd, M. P.; Islam, M. M.; Strachan, A. Sensitivity of the Shock Initiation Threshold of 1,3,5-Triamino-2,4,6-Trinitrobenzene (TATB) to Nuclear Quantum Effects. *J. Phys. Chem. C* **2019**, *123* (36), 21969–21981.

(32) Guo, D.; Zybin, S. V.; An, Q.; Goddard, W. A.; Huang, F. Prediction of the Chapman-Jouguet Chemical Equilibrium State in a Detonation Wave from First Principles Based Reactive Molecular Dynamics. *Phys. Chem. Chem. Phys.* **2016**, *18* (3), 2015–2022.

(33) Islam, M. M.; Strachan, A. Decomposition and Reaction of Polyvinyl Nitrate under Shock and Thermal Loading: A ReaxFF Reactive Molecular Dynamics Study. *J. Phys. Chem. C* **2017**, *121* (40), 22452–22464.

(34) Islam, M. M.; Strachan, A. Reactive Molecular Dynamics Simulations to Investigate the Shock Response of Liquid Nitromethane. *J. Phys. Chem. C* **2019**, *123* (4), 2613–2626.

(35) Powell, M. S.; Sakano, M. N.; Cawkwell, M. J.; Bowlan, P. R.; Brown, K. E.; Bolme, C. A.; Moore, D. S.; Son, S. F.; Strachan, A.; McGrane, S. D. Insight into the Chemistry of PETN

under Shock Compression through Ultrafast Broadband Mid-Infrared Absorption Spectroscopy. *J. Phys. Chem. A* **2020**, *124* (35), 7031–7046.

(36) Zhang, L.; Zybin, S. V; Duin, A. C. T. Van; Dasgupta, S.; Iii, W. A. G.; Kober, E. M. High Explosives from ReaxFF Reactive Molecular Dynamics Simulations. *Society* **2009**, 10619–10640.

(37) Hamilton, B. W.; Steele, B. A.; Sakano, M. N.; Kroonblawd, M. P.; Kuo, I. F. W.; Strachan, A. Predicted Reaction Mechanisms, Product Speciation, Kinetics, and Detonation Properties of the Insensitive Explosive 2,6-Diamino-3,5-Dinitropyrazine-1-Oxide (LLM-105). *J. Phys. Chem. A* **2021**, *125* (8), 1766–1777.

(38) Wu, C. J.; Fried, L. E. Ab Initio Study of RDX Decomposition Mechanisms. *J. Phys. Chem. A* **1997**, *101* (46), 8675–8679.

(39) Wu, C. J.; Fried, L. E. Ring Closure Mediated by Intramolecular Hydrogen Transfer in the Decomposition of a Push-Pull Nitroaromatic: TATB. *J. Phys. Chem. A* **2000**, *104* (27), 6447–6452.

(40) Sakano, M.; Hamilton, B. W.; Islam, M. M.; Strachan, A. Role of Molecular Disorder on the Reactivity of RDX. *J. Phys. Chem. C* **2018**, *122* (47), 27032–27043.

(41) Sakano, M. N.; Hamed, A.; Kober, E. M.; Grilli, N.; Hamilton, B. W.; Islam, M. M.; Koslowski, M.; Strachan, A. Unsupervised Learning-Based Multiscale Model of Thermochemistry in 1,3,5-Trinitro-1,3,5-Triazinane (RDX). *J. Phys. Chem. A* **2020**, *124* (44), 9141–9155.

(42) Wood, M. A.; Cherukara, M. J.; Kober, E. M.; Strachan, A. Ultrafast Chemistry under Nonequilibrium Conditions and the Shock to Deflagration Transition at the Nanoscale. *J. Phys. Chem. C* **2015**, *119* (38), 22008–22015.

(43) Shan, T. R.; Wixom, R. R.; Thompson, A. P. Extended Asymmetric Hot Region Formation Due to Shockwave Interactions Following Void Collapse in Shocked High Explosive. *Phys. Rev. B* **2016**, *94* (5).

(44) Kroonblawd, M. P.; Fried, L. E. High Explosive Ignition through Chemically Activated Nanoscale Shear Bands. *Phys. Rev. Lett.* **2020**, *124* (20), 206002.

(45) Fried, L. E. High Explosive Shock Initiation Model Based on Hot Spot Temperature. *Proc. 16th Int. Detonation Symp.* **2018**, 1156–1163.

(46) Hamilton, B. W.; Kroonblawd, M. P.; Li, C.; Strachan, A. A Hotspot's Better Half: Non-Equilibrium Intra-Molecular Strain in Shock Physics. *J. Phys. Chem. Lett.* **2021**, *12* (11), 2756–2762.

(47) Kroonblawd, M. P.; Hamilton, B. W.; Strachan, A. Fourier-like Thermal Relaxation of Nanoscale Explosive Hot Spots. *J. Phys. Chem. C* **2021**, *125*, 20570–20582.

(48) Ribas-Arino, J.; Marx, D. Covalent Mechanochemistry: Theoretical Concepts and Computational Tools with Applications to Molecular Nanomechanics. *Chem. Rev.* **2012**, *112* (10), 5412–5487.

(49) Islam, M. M.; Strachan, A. Role of Dynamical Compressive and Shear Loading on Hotspot

Criticality in RDX via Reactive Molecular Dynamics. *J. Appl. Phys.* **2020**, *128* (6).

(50) Wiita, A. P.; Ainavarapu, S. R. K.; Huang, H. H.; Fernandez, J. M. Force-Dependent Chemical Kinetics of Disulfide Bond Reduction Observed with Single-Molecule Techniques. *Proc. Natl. Acad. Sci. U. S. A.* **2006**, *103* (19), 7222–7227.

(51) Stauch, T.; Dreuw, A. Advances in Quantum Mechanochemistry: Electronic Structure Methods and Force Analysis. *Chem. Rev.* **2016**, *116* (22), 14137–14180.

(52) Ong, M. T.; Leiding, J.; Tao, H.; Virshup, A. M.; Martínez, T. J. First Principles Dynamics and Minimum Energy Pathways for Mechanochemical Ring Opening of Cyclobutene. *J. Am. Chem. Soc.* **2009**, *131* (18), 6377–6379.

(53) Kroonblawd, M. P.; Steele, B. A.; Nelms, M. D.; Fried, L. E.; Austin, R. A. Anisotropic Strength Behavior of Single-Crystal TATB. *Model. Simul. Mater. Sci. Eng.* **2021**.

(54) Cady, H. H.; Larson, A. C. The Crystal Structure of 1,3,5-Triamino-2,4,6-Trinitrobenzene. *Acta Crystallogr.* **1965**, *18* (3), 485–496.

(55) Lafourcade, P.; Denoual, C.; Maillet, J. B. Irreversible Deformation Mechanisms for 1,3,5-Triamino-2,4,6-Trinitrobenzene Single Crystal through Molecular Dynamics Simulations. *J. Phys. Chem. C* **2018**, *122* (26), 14954–14964.

(56) Zhao, P.; Kroonblawd, M. P.; Mathew, N.; Sewell, T. Strongly Anisotropic Thermomechanical Response to Shock Wave Loading in Oriented Samples of the Triclinic Molecular Crystal 1,3,5- Triamino-2,4,6-Trinitrobenzene. *J. Phys. Chem. C* **2021**, *125*, 22747–22765.

(57) Kroonblawd, M. P.; Sewell, T. D. Theoretical Determination of Anisotropic Thermal Conductivity for Initially Defect-Free and Defective TATB Single Crystals. *J. Chem. Phys.* **2014**, *141* (18).

(58) Steele, B. A.; Clarke, S. M.; Kroonblawd, M. P.; Kuo, I. F. W.; Pagoria, P. F.; Tkachev, S. N.; Smith, J. S.; Bastea, S.; Fried, L. E.; Zaug, J. M.; et al. Pressure-Induced Phase Transition in 1,3,5-Triamino-2,4,6-Trinitrobenzene (TATB). *Appl. Phys. Lett.* **2019**, *114* (19).

(59) Bassett, W. P.; Johnson, B. P.; Neelakantan, N. K.; Suslick, K. S.; Dlott, D. D. Shock Initiation of Explosives: High Temperature Hot Spots Explained. *Appl. Phys. Lett.* **2017**, *111* (6).

(60) Bassett, W. P.; Johnson, B. P.; Dlott, D. D. Dynamic Absorption in Optical Pyrometry of Hot Spots in Plastic-Bonded Triaminotrinitrobenzene. *Appl. Phys. Lett.* **2019**, *114* (19).

(61) Bassett, W. P.; Johnson, B. P.; Salvati, L.; Nissen, E. J.; Bhowmick, M.; Dlott, D. D. Shock Initiation Microscopy with High Time and Space Resolution. *Propellants, Explos. Pyrotech.* **2020**, *45* (2), 223–235.

(62) Plimpton, S. Fast Parallel Algorithms for Short-Range Molecular Dynamics. *Journal of Computational Physics*. 1995, pp 1–19.

(63) Bedrov, D.; Borodin, O.; Smith, G. D.; Sewell, T. D.; Dattelbaum, D. M.; Stevens, L. L. A Molecular Dynamics Simulation Study of Crystalline 1,3,5-Triamino-2,4,6- Trinitrobenzene as a Function of Pressure and Temperature. *J. Chem. Phys.* **2009**, *131* (22).

(64) Kroonblawd, M. P.; Sewell, T. D. Theoretical Determination of Anisotropic Thermal Conductivity for Crystalline 1,3,5-Triamino-2,4,6-Trinitrobenzene (TATB). *J. Chem. Phys.* **2013**, *139* (7).

(65) Andersen, H. C. Rattle: A "Velocity" Version of the Shake Algorithm for Molecular Dynamics Calculations. *J. Comput. Phys.* **1983**, *52* (1), 24–34.

(66) Mathew, N.; Sewell, T. D.; Thompson, D. L. Anisotropy in Surface-Initiated Melting of the Triclinic Molecular Crystal 1,3,5-Triamino-2,4,6-Trinitrobenzene: A Molecular Dynamics Study. *J. Chem. Phys.* **2015**, *143* (9).

(67) Wolf, D.; Keblinski, P.; Phillpot, S. R.; Eggebrecht, J. Exact Method for the Simulation of Coulombic Systems by Spherically Truncated, Pairwise r-1 Summation. *J. Chem. Phys.* **1999**, *110* (17), 8254–8282.

(68) Kroonblawd, M. P.; Mathew, N.; Jiang, S.; Sewell, T. D. A Generalized Crystal-Cutting Method for Modeling Arbitrarily Oriented Crystals in 3D Periodic Simulation Cells with Applications to Crystal–Crystal Interfaces. *Comput. Phys. Commun.* **2016**, *207*, 232–242.

(69) Nosé, S. A Unified Formulation of the Constant Temperature Molecular Dynamics Methods. *J. Chem. Phys.* **1984**, *81* (1), 511–519.

(70) Holian, B. L.; Lomdahl, P. S. Plasticity Induced by Shock Waves in Nonequilibrium Molecular-Dynamics Simulations. *Science (80-.).* **1998**, *280* (5372), 2085–2088.

(71) Taw, M. R.; Yeager, J. D.; Hooks, D. E.; Carvajal, T. M.; Bahr, D. F. The Mechanical Properties of As-Grown Noncubic Organic Molecular Crystals Assessed by Nanoindentation. *J. Mater. Res.* **2017**, *32* (14), 2728–2737.

(72) Pal, A.; Picu, C. R. Non-Schmid Effect of Pressure on Plastic Deformation in Molecular Crystal HMX. *J. Appl. Phys.* **2019**, *125* (21), 1–9.

(73) Forbes, J. W. *Shock Wave Compression of Condensed Matter*; Springer Science & Business Media, 2013.

(74) Sturtevant, B.; Kulkarny, V. A. The Focusing of Weak Shock Waves. *J. Fluid Mech.* **1976**, *73* (4), 651–671.

(75) Cates, J. E.; Sturtevant, B. Shock Wave Focusing Using Geometrical Shock Dynamics. *Phys. Fluids* **1997**, *9* (10), 3058–3068.

(76) Tarver, C. M.; Chidester, S. K.; Nichols, A. L. Critical Conditions for Impact- and Shock-Induced Hot Spots in Solid Explosives. *J. Phys. Chem.* **1996**, *100* (14), 5794–5799.

(77) Manaa, M. R.; Reed, E. J.; Fried, L. E.; Goldman, N. Nitrogen-Rich Heterocycles as Reactivity Retardants in Shocked Insensitive Explosives. *J. Am. Chem. Soc.* **2009**, *131* (15), 5483–5487.

(78) Tiwari, S. C.; Nomura, K. I.; Kalia, R. K.; Nakano, A.; Vashishta, P. Multiple Reaction Pathways in Shocked 2,4,6-Triamino-1,3,5-Trinitrobenzene Crystal. *J. Phys. Chem. C* **2017**, *121* (29), 16029–16034.

(79) Manaa, M. R.; Gee, R. H.; Fried, L. E. Internal Rotation of Amino and Nitro Groups in TATB: MP2 versus DFT (B3LYP). *J. Phys. Chem. A* **2002**, *106* (37), 8806–8810.

ToC Graphic

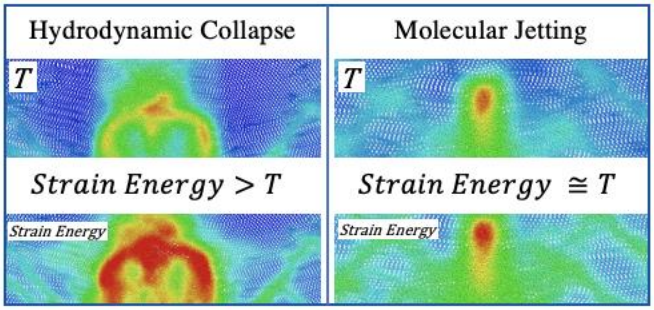
Hydrodynamic Collapse
Molecular Jetting
T
T
Strain Energy > T
Strain Energy ≅ T
Strain Energy
Strain Energy

Supplemental Materials to: The Potential Energy Hotspot: Effects from Impact Velocity, Defect Geometry, and Crystallographic Orientation

Brenden W. Hamilton[1], Matthew P. Kroonblawd[2], Alejandro Strachan[1]*

[1]School of Materials Engineering and Birck Nanotechnology Center, Purdue University, West Lafayette, Indiana, 47907 USA
[2]Physical and Life Sciences Directorate, Lawrence Livermore National Laboratory, Livermore, California 94550, United States
strachan@purdue.edu

SM-1: Diamond Pore Ejecta Velocity Distribution

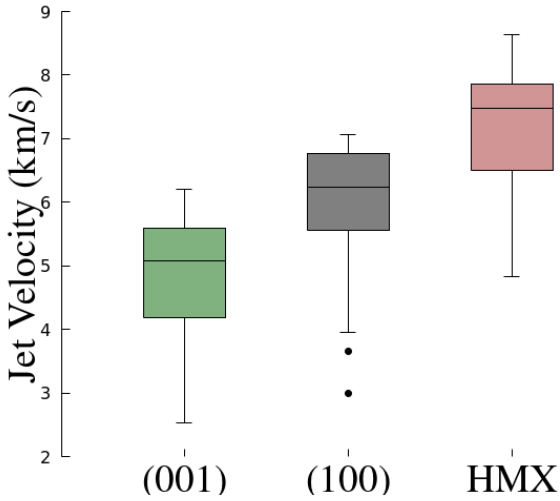

Figure S1: Box and whisker plot of the velocities of ejected molecules for the (001) crack, (100) crack, and an HMX crack, all at a particle velocity of 2.0 km/s.

SM-2: Diamond Pore Ejecta Time Evolution

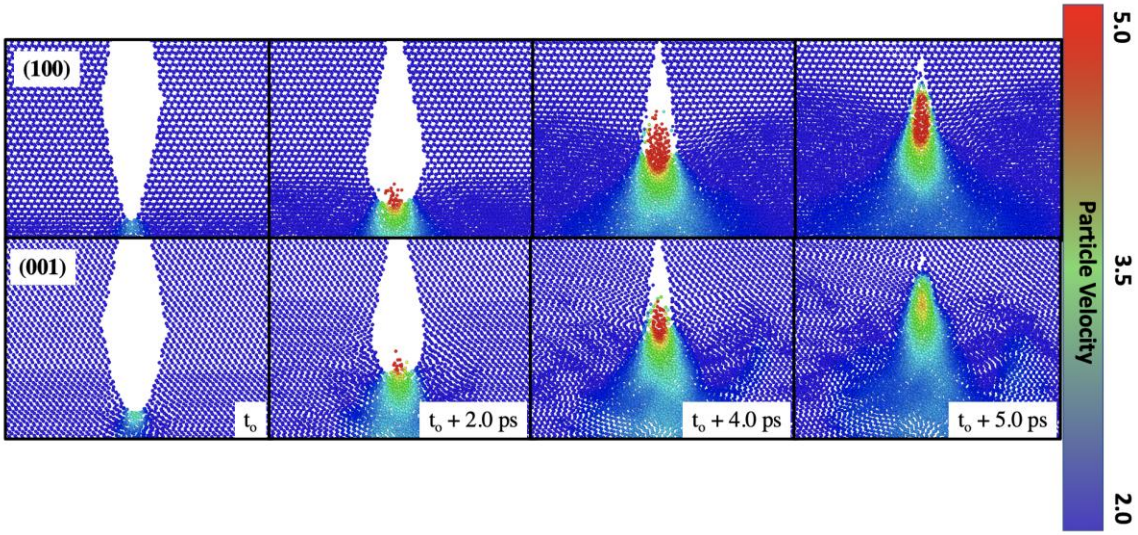

Figure S2: Time evolution of molecular ejecta for both the (100) and (001) diamond pores for shocks of $U_p = 2.0\ km/s$.

SM-3: Spatial Localization of PE

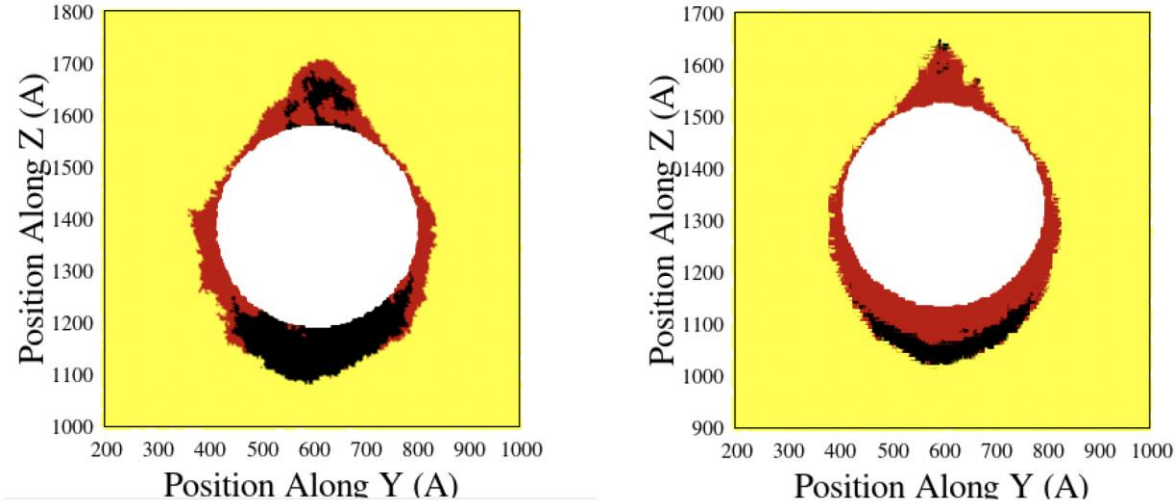

Figure S3: Initial positions of region atoms from Figure 10 in the main manuscript.